

A Sensitivity Study of the Effect of Image Resolution on Predicted Petrophysical Properties

Nayef Alyafei¹ · Ali Qaseminejad Raeini¹ ·
Adriana Paluszny¹ · Martin J. Blunt¹

Received: 3 June 2014 / Accepted: 6 August 2015 / Published online: 1 September 2015
© Springer Science+Business Media Dordrecht 2015

Abstract Micro-CT scanning is a nondestructive technique that can provide three-dimensional images of rock pore structure at a resolution of a few microns. We compute petrophysical properties on three-dimensional images of benchmark rocks: two sandstones (Berea and Doddington) and two limestones (Estailades and Ketton). We take scans at a voxel size of approximately $2.7\ \mu\text{m}$ and with 1024^3 voxels for both sandstone and limestone rocks. We numerically upscale the images to image sizes of 512^3 , 256^3 and 128^3 , representing voxel sizes of around 5.4, 10.8, and $21.6\ \mu\text{m}$ respectively, covering the same domains with coarser resolution. We calculate porosity and permeability on these images by using direct simulation and by extracting geometrical equivalent networks. We find that the predicted porosity is fairly insensitive to resolution for sandstones studied with the selected range of resolutions but sensitive for limestones with lower porosity for larger voxel sizes. For the permeability predictions, we do not observe a clear trend in permeability as a function of voxel size; however, sandstones, roughly, have comparable permeability regardless of the voxel size. On the other hand, for limestones, we generally see a decreasing trend in permeability as a function of upscaled voxel size.

Keywords Pore-scale modeling · Image resolution · Petrophysics · Micro-CT · Upscaling

1 Introduction

Advances in three-dimensional digital imaging have allowed direct visualization of the pore space of many rocks (Dunsmuir et al. 1991; Lindquist and Venkatarangan 1999; Thovet et al. 2001; Wildenschild et al. 2002, 2005; Wildenschild and Sheppard 2013). Pore-scale imaging and modeling has received enormous attention in recent years, since it offers the promise to predict flow and transport properties using three-dimensional images of the pore space (see,

✉ Nayef Alyafei
nmalyafei@gmail.com; nayef.alyafei@qatar.tamu.edu

¹ Department of Earth Science and Engineering, Imperial College London, London SW7 2AZ, UK

for instance, Blunt et al. 2013). However, the quality of the predictions is, clearly, related to the resolution of the images used as a basis for these calculations (Arns et al. 2002; Wildenschild et al. 2005). There is, furthermore, an inevitable trade-off between image resolution and the overall size of the system that can be modeled.

In conventional reservoir simulation models, having more cells is thought to capture heterogeneity more accurately to obtain more reliable predictions of oil recovery. However, at some point, simulation becomes impractical and resource-intensive as the size of the model is increased. Similarly, we can compare lowering image resolution to upscaling in reservoir simulation: We upscale in order to reduce the computational time with a deterioration of the model's accuracy. However, what resolution is necessary to be representative of the rock at the pore scale?

There are few studies in the literature on the effect of image resolution. Peng et al. (2012) performed a study on Berea sandstone with two resolutions of 0.35 and 12.7 μm . They studied porosity, pore size distribution, pore connectivity, surface area, hydraulic radius, and aspect ratio. They found that the high-resolution image was better able to capture the pore size; however, since they took a smaller volume for the high-resolution images for the analysis, they found the larger, lower-resolution images represented large pores more accurately. Alyafei et al. (2013) studied five different resolution images ($\approx 6\text{--}20\ \mu\text{m}$) for two different sandstones and demonstrated an insensitivity of porosity to image resolution, while permeability varied considerably. Arns et al. (2005) performed a study on a reservoir carbonate where they showed that the porosity is very sensitive to image resolution: It reduced from 11.2 % at 2.5 μm to 3.2 % at 20 μm . Keemhm and Mukerji (2004) performed a study on image resolution on Fontainebleau sandstone, and they found that that porosity is insensitive to spatial resolution while predicted permeability increases at very low spatial resolutions.

There are two approaches to compute flow and transport based on three-dimensional representations of the pore space. The first is to compute the flow field directly on images using finite difference or particle-based methods (Gerbaux et al. 2010; Mostaghimi et al. 2012; Raeini et al. 2014; Ramstad et al. 2012; Spanne et al. 1994). The second approach to extract network of pores and throats and compute flow using quasi-static pore network models (Silin et al. 2003; Al-Kharusi and Blunt 2007; Dong and Blunt 2009). While the second approach simplifies the geometry of the pore space, it enables displacement in each network element to be computed semi-analytically. It is very efficient for the determination of multi-phase flow properties where capillary forces dominate (Øren and Bakke 2002; Valvatne and Blunt 2004; Ryazanov et al. 2009). In this paper we will use both methods to predict permeability, and the network approach to determine pore and throat size distributions and connectivity.

In this paper, we will quantify the level of uncertainty related to upscaling micro-CT images on predictions of petrophysical properties using pore-scale simulation. We obtained scans with the maximum resolution of the micro-CT scanner and then used averaging methods and linear interpolation to upscale our images. Then we compare, as a function of resolution, network structures (number of pores, number of throats, average pore radius, average throat radius, and coordination number), and single-phase properties (porosity and permeability). Where available, we compare the predictions with experimental data.

2 Experimental Methodology

We study four quarry rocks: Berea and Doddington sandstones and Estailades and Ketton limestones. Berea is from the Berea quarry in Ohio, USA. It is of Mississippian age and

consists of 87.3 % quartz, 4.2 % kaolinite, 3.2 % mica and 3 % K-feldspar (Pepper et al. 1954). Doddington is from the Doddington quarry in Wooler, UK. It is from the Carboniferous period and nonfossiliferous, and consists of 93.6 % quartz, 1.9 % kaolinite, 2 % mica and 1.7 % K-feldspar (Santarelli and Brown 1989). Estailades is from the Estailade Formation, found in the Oppède quarry, south of France. It is from the Cenomanian and Campanian ages and consists of 99 % calcite; the remaining 1 % accounts for traces of dolomite and silica (Wright et al. 1995). Ketton is from the Lincolnshire Formation, located in Rutland, east Midlands, UK. It is from the Toarcian and Bajocian ages and consists of 99.1 % calcite and 0.9 % quartz (Ashton 1980).

Basic properties, such as porosity and brine permeability of the rocks measured on standard cylindrical cores (diameter 38.1 mm, length 75 mm) via Helium pycnometry and a Hassler-type cell with cylindrical confining pressure, respectively, are found and shown in Table 1. We dry-scanned smaller cylindrical cores (diameter 4.95 mm, length 10 mm) using an Xradia Versa 500 micro-CT scanner at iRock Technologies, Beijing, China. To guarantee consistency, the small and large cores were drilled out of the same block. Furthermore, we sent rock samples for mercury injection capillary pressure (MICP) measurements (Autopore IV 9520, Weatherford Laboratories, East Grinstead, UK).

From the MICP, we can estimate the pore throat radii using the Young–Laplace equation:

$$P_c = \frac{2\sigma \cos \theta}{r_p} \quad (1)$$

where P_c is the capillary pressure, σ is the interfacial tension, 480 mN m^{-1} for the mercury/air system. θ is the contact angle, 40° , and r_p is the pore throat radius. From the MICP curves in Fig. 1, we can see that Berea has highest capillary entry pressure, with a minimum value of $P_c/2\sigma \cos \theta$ in units of μm^{-1} , of approximately $0.04 \mu\text{m}^{-1}$ with an equivalent r_p of $24 \mu\text{m}$. Estailades has a lower capillary entry pressure of approximately $0.029 \mu\text{m}^{-1}$ with an equivalent r_p of $35 \mu\text{m}$. Doddington has a lower capillary entry pressure than Estailades of approximately $0.026 \mu\text{m}^{-1}$ with an equivalent r_p of $38 \mu\text{m}$. Ketton has the lowest capillary entry pressure of approximately $0.017 \mu\text{m}^{-1}$ with an equivalent r_p of $59 \mu\text{m}$ (Tanino and Blunt 2012).

This can be further interpreted by using the probability distribution function (f) of (r_p) (Dullien 1992):

$$r_p f(r_p) = r_p \frac{dS_w}{dr_p} = -P_c \frac{dS_w}{dP_c} = -\frac{dS_w}{d \ln P_c} \quad (2)$$

From this distribution, Fig. 2, we can see that both sandstones have a distinct uni-modal distribution with the majority of the pore sizes greater than $1 \mu\text{m}$, while Estailades and Ketton have a distinct bimodal distribution with around half of the pore sizes less than $1 \mu\text{m}$.

Table 1 Basic measured petrophysical properties for the rocks used in this study

Rock	Image size (voxel)	Voxel size (μm)	Porosity (ϕ) (%)	Permeability (k) ($\times 10^{-13} \text{ m}^2$)
Berea	1024^3	2.77	21	5.6
Doddington	1024^3	2.69	22	15.8
Estailades	1024^3	2.68	28	1.8
Ketton	1024^3	2.65	23	25.4

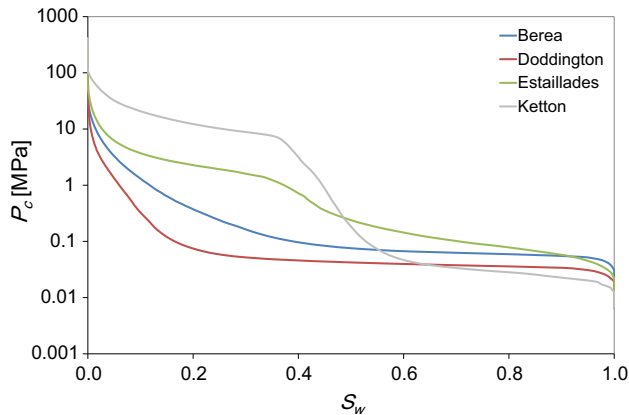


Fig. 1 Measured capillary pressures (mercury/air) as a function of equivalent water saturation, S_w , for all the rocks

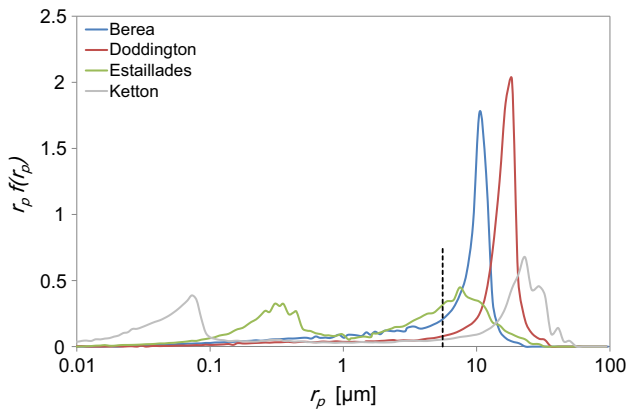


Fig. 2 The pore size distribution against pore throat radius for all the rocks. The dashed line depicts $r_p = 2.7 \mu\text{m}$

From the $2.7 \mu\text{m}$ dashed line in Fig. 2 (which represents approximately the average voxel size of all the rocks), the vast majority of the pore space can be resolved for the sandstones and around half of the pore spaces can be resolved for the limestones. Since Estailades and Ketton are carbonate rocks, approximately half of their porosities are considered to be intra-granular microporosity which cannot be resolved by the micro-CT which requires an instrument with nm resolution.

3 Image Processing

We crop each grayscale image to a cubic base case of 1024^3 voxels which is equivalent to a volume of 22.8, 20.9, 20.7, and 20.0 mm^3 for Berea, Doddington, Estailades, and Ketton, respectively. Then, we segment the images by applying a three-step method (Iglauer et al. 2011, 2013): (1) We clean CT images of ring artifacts by applying a stripe removal algorithm based on combined wavelet—Fourier filtering (Münch et al. 2009); (2) We apply a conservative anisotropic regularization filter to reduce salt-and-pepper noise (Tschumperlé and Deriche 2005). At this stage the following parameters are used: The parameters for

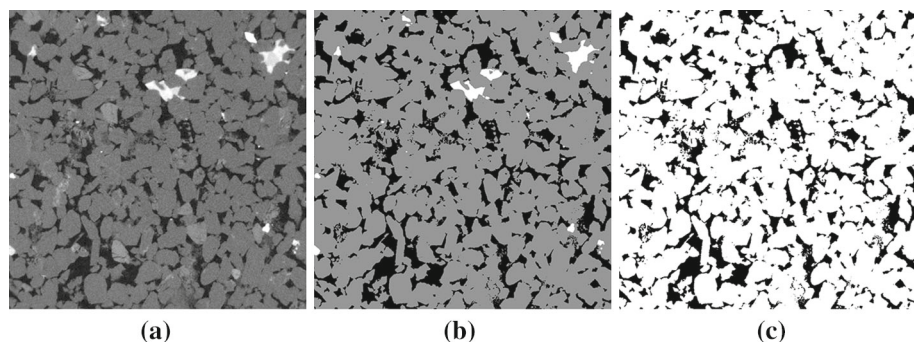


Fig. 3 Cross section of **a** grayscale micro-CT image, **b** three-phase multi-thresholding, and **c** two-phase image segmentation for the 1024^3 voxel image of Berea sandstone

the anisotropic filter are as follows. A total of five smoothing iterations per image is performed, with the diffusion limiter along minimal and maximal variations set to 0.50 and 0.90, respectively, and an edge threshold height of 2.5. The Otsu segmentation is based on the identification of five peaks, and these are later classified into pore and grain based on topological connectivity. The five peaks capture grains and pores, and high density inclusions which appear as bright grains in the samples. (3) We segment pore and grain domains according to peaks in the gray level histograms, using Otsu's multi-thresholding (Otsu 1979). Furthermore, due to their fine resolution and the presence of clay with high X-ray absorption, we subdivided the images into three domains, for which the brightest corresponded to the clay inclusions, Fig. 3. Figure 4 shows segmented three-dimensional images of each rock.

Then, we re-sample/upscale each image on the (x, y) axes directly from the segmented images by factors of 2, 4, and 8 using the Lanczos re-sampling algorithm, Figs. 5 and 6. Lanczos is a windowed downsampling interpolation method which performs a local average over specific finite window (i.e., binning) by averaging distance with the first oscillation of the sinc() function. Lanczos prevents the artificial formation of Moiré effects and reduces the level of detail without artificially sharpening the image (Duchon 1979). We downsample the dataset on a pixel by pixel basis in the z direction by applying uniform averaging. This is in order to preserve the same physical volume as the 1024^3 data set and thus to have a standard comparison between all the cases. The resizing of the dataset is always performed in the downsampling sense. Thus, the largest image corresponds to the highest resolution image. The current method corresponds to the slab-averaging technique which is used in the medical imaging context, and is known to preserve the level of detail without introducing unwanted artifacts to the image. Upscaling in the vertical, z , direction is a function of the spacing and amount of averaged slides in the z direction. If the averaging is performed indiscriminately, this can result in anisotropic sampling of the dataset. However, the present case is simple in that upscaling reduces the dimension of the dataset by half in each case. Thus, in each step, two pixels were averaged in the z direction after applying the Lanczos filter. The result is a set of datasets of decreasing resolutions: 1024^3 , 512^3 , 256^3 , and 128^3 representing voxel sizes of 2.77, 5.54, 11.08, and 22.16 μm for Berea, 2.69, 5.38, 10.76, and 21.52 μm for Doddington, 2.68, 5.36, 10.72, and 21.44 μm for Estaillades, and 2.65, 5.3, 10.6, and 21.2 μm for Ketton.

We include all the segmented images used in this study in an online library available for download.¹

¹ The images used in this study can be downloaded from <http://www.imperial.ac.uk/engineering/departments/earth-science/research/research-groups/perm/research/pore-scale-modelling/micro-ct-images-and-networks/>.

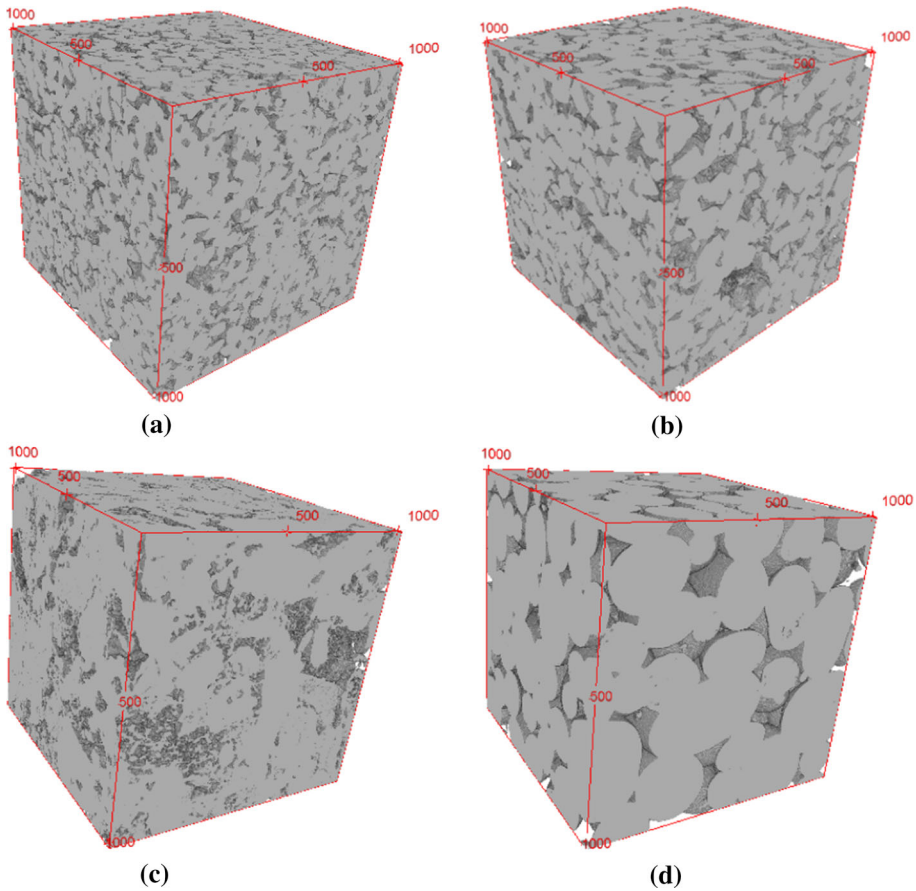


Fig. 4 Segmented three-dimensional micro-CT images for **a** Berea, **b** Doddington, **c** Estailades and **d** Ketton representing 1024^3 voxels

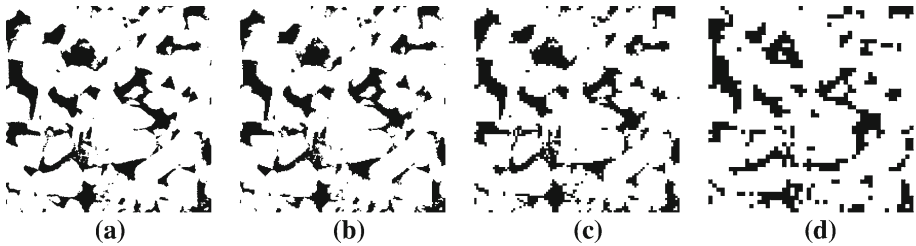


Fig. 5 Small region of 2D cross section of Berea sandstone of **a** 1024×1024 pixel², **b** after upscaling to 512×512 pixel², **c** after upscaling to 256×256 pixel², and **d** after upscaling to 128×128 pixel²

4 Network Structures

We use a maximal ball algorithm to extract networks from the images. The method finds the largest spheres that fit in the pore space are pores, while chains of smaller spheres connecting them represent throats. Details of the method are provided elsewhere ([Dong and Blunt 2009](#)).

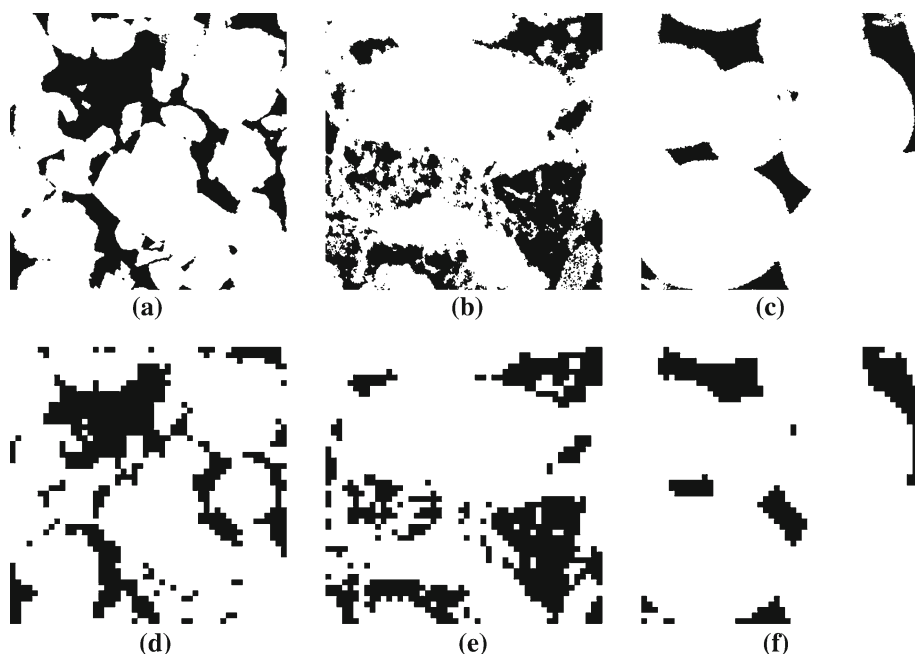


Fig. 6 A 2D portion of the high-resolution (1024^3) image of **a** Doddington, **b** Estailades, and **c** Ketton. The equivalent portion of the lowest resolution (128^3) image of **d** Doddington, **e** Estailades, and **f** Ketton

Figure 7 shows three-dimensional images of the extracted pores and throats. We compare the rocks in terms of numbers of pores, throats, average pore radius, average throat radius, and coordination numbers (average number of throats connected to each pore).

Tables 2 and 3 show the network properties of the rocks. We can see that Estailades has the highest number of pores and throats, while Ketton has the lowest. From Fig. 4, we can see that Estailades is characterized with both large and small pores, while Ketton has only few big pores that can be captured by micro-CT imaging. Similarly, Doddington is characterized by larger pores compared with Berea. Network extraction does not produce unique networks with more small pores and throats as the resolution becomes finer. Ketton has the largest average pore and throat radii which might be expected due to its high permeability. Both average pore and throat radii decrease as we decrease voxel size for all the rocks. Estailades has the highest average coordination number; this can be explained by the large number of small throats that contribute to the connectivity of the rock. The coordination number shows opposite trends for sandstones than limestones. For sandstones, the coordination number increases as we increase the voxel size, while we see a decrease for Estailades and little change for Ketton.

The computed pore and throat radii distribution from the extracted networks are shown in Figs. 8 and 9, respectively. Note that we do not capture microporosity in these images and hence cannot accommodate elements smaller than a few μm in size. This explains the unimodal distribution of these figures, unlike the MICP measurements. The pore and throat size distributions peak close the voxel size. In most of the cases, network extraction underestimates the macro-pores compared to MICP which has the highest resolution, covering a wider range of throat sizes.

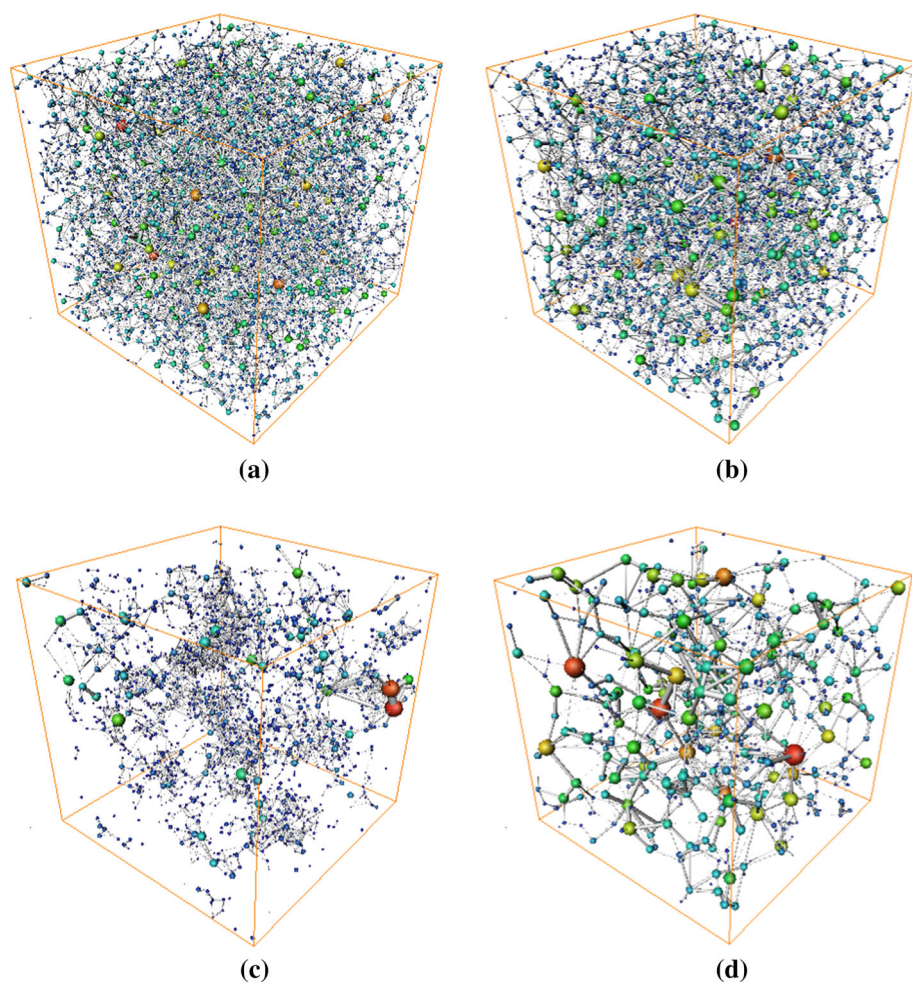


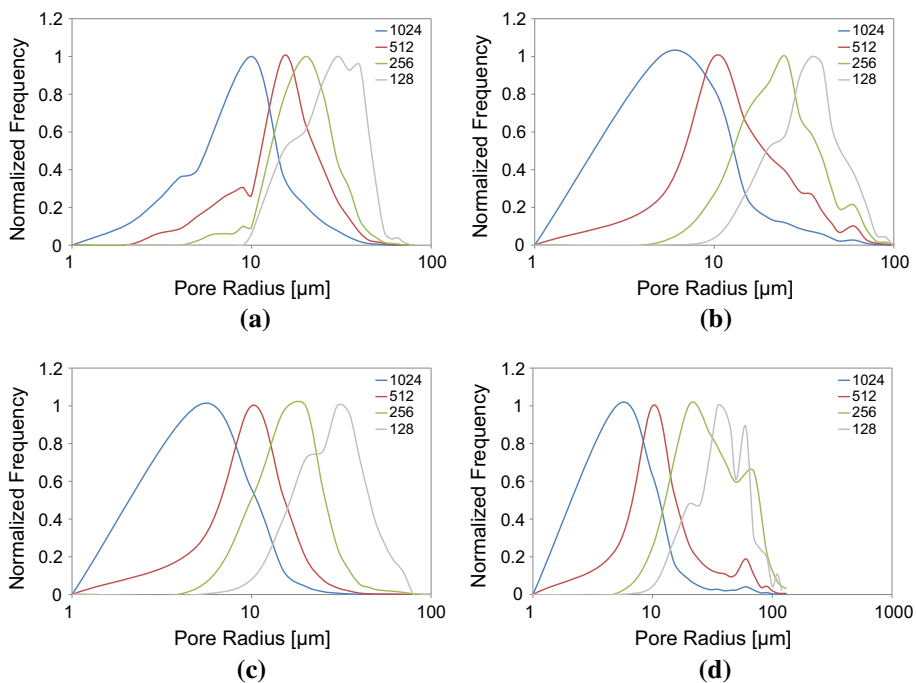
Fig. 7 Three-dimensional pore and throat images [generated from a network extraction code (Dong and Blunt 2009)] of **a** Berea, **b** Doddington, **c** Estaillades, and **d** Ketton. The images shown are for 256^3 voxel images

Table 2 Network structure properties for the two sandstones

Image size (voxel)	Berea				Doddington			
	1024^3	512^3	256^3	128^3	1024^3	512^3	256^3	128^3
Number of pores	39937	14878	5432	1056	38390	6233	2991	1131
Number of throats	81155	35820	15400	4244	69271	15085	8087	3762
Average pore radius (μm)	9.0	14.4	20.5	29.9	11.1	19.2	27.0	35.0
Average throat radius (μm)	4.3	5.9	8.0	12.9	5.4	8.1	10.4	13.9
Coordination number	4.0	4.8	5.59	7.9	3.6	4.8	5.3	6.5

Table 3 Network structure properties for the two limestones

Image size (voxel)	Estailades				Ketton			
	1024 ³	512 ³	256 ³	128 ³	1024 ³	512 ³	256 ³	128 ³
Number of pores	88772	15557	2166	148	19827	1615	694	335
Number of throats	243251	41072	5162	190	36362	3572	1526	624
Average pore radius (μm)	5.8	10.5	17.8	31.5	10.7	22.5	35.1	41.0
Average throat radius (μm)	2.7	4.6	7.8	14.9	5.9	10.0	14.6	16.3
Coordination number	5.5	5.2	4.7	2.4	3.7	4.3	4.2	3.5

**Fig. 8** Normalized pore radius distribution from the extracted networks for different resolutions for **a** Berea, **b** Doddington, **c** Estailades, and **d** Ketton

5 Single-Phase Properties

The image porosity is relatively insensitive to resolution for both sandstone rocks, Table 4. The computed values, based on the thresholded images, are close to the experimentally measured values. However, for the limestones there is a clear increase in the image porosity as a function of voxel size. In addition, even with the largest voxel size, we can only capture up to 60–66% of the porosity, indicating that micro-CT imaging is not able to resolve the microporosity adequately.

We then calculate the permeability using two methods. First we compute flow at low Reynold's number directly on the images using a finite difference Stokes-flow simulator (Raeini et al. 2014). Second we use the extracted networks. This computation essentially

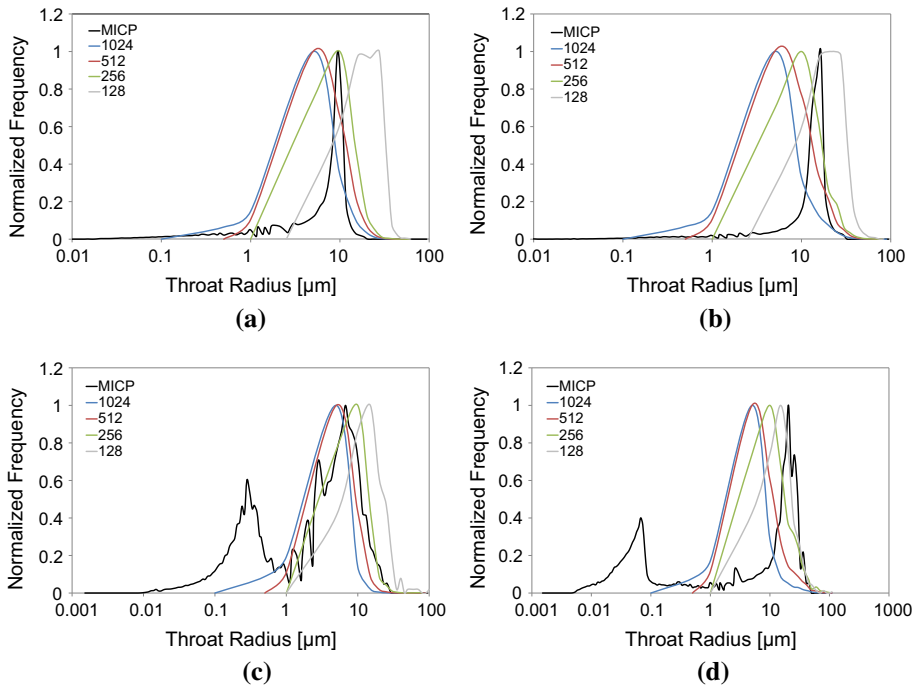


Fig. 9 Normalized throat radius distribution from the extracted networks for different resolutions for **a** Berea, **b** Doddington, **c** Estailades, and **d** Ketton compared to the MICP pore throat radius

Table 4 Image porosity for all the rocks used in this study where ϕ_{Image}/ϕ is the ratio of the image porosity to the experimental value of the large cores

Image size (voxel)	$\phi_{\text{Image}} (\%)$				$\phi_{\text{Image}}/\phi (\%)$			
	1024 ³	512 ³	256 ³	128 ³	1024 ³	512 ³	256 ³	128 ³
Berea	20.2	20.2	20.1	20.0	96.2	96.2	95.7	95.2
Doddington	21.7	21.6	21.6	21.6	98.6	98.2	98.2	98.2
Estailades	16.9	13.3	8.6	3.7	60.4	47.5	30.7	13.2
Ketton	15.2	14.0	12.5	9.7	66.1	60.9	54.3	42.2

treats the porous medium as a random resistor network with semi-analytically computed flow conductances for each element (Valvatne and Blunt 2004).

Figure 10 shows the predicted permeability using direct simulation and the extracted networks as a function of voxel size for all the rocks. For the sandstones the predicted permeabilities are generally comparable using the two methods and seem to be independent of the voxel resolution, except for the 128³ voxel image using the network approach for Berea sandstone where the permeability is over-predicted.

For the limestones, we observe an increasing trend between the permeability and number of voxels, which indicates that capturing more features of the limestones will result in higher permeability. These small pores contribute to the connectivity. For Estailades, the 128³ image size is too poor to capture the features of the rock morphology, and did not result

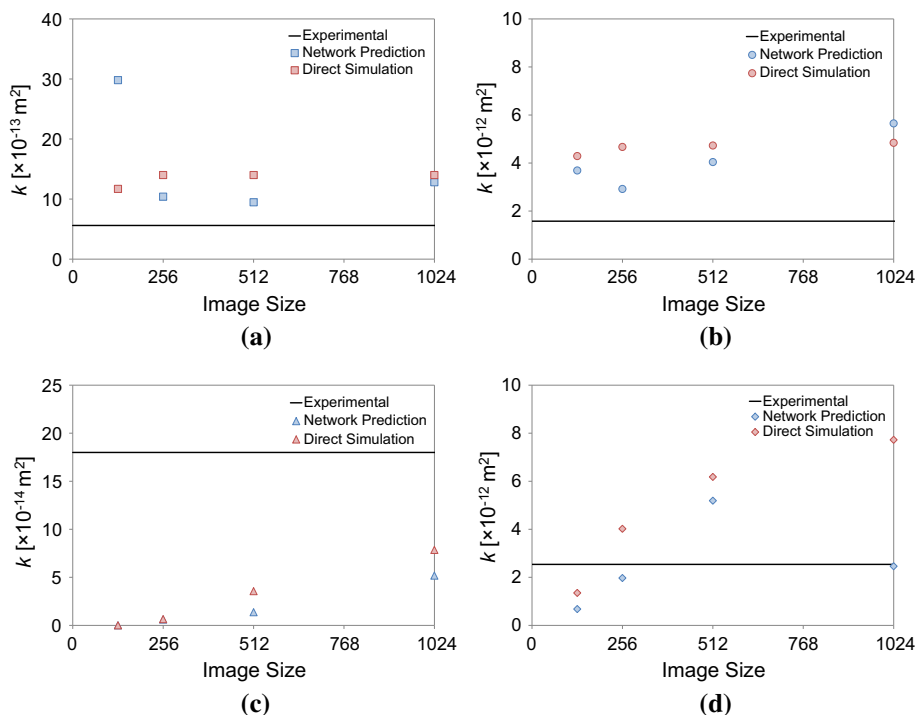


Fig. 10 Predicted permeability for **a** Berea, **b** Doddington, **c** Estailades, and **d** Ketton, compared to the experimental value

in a connected pore space, giving a zero permeability. The results indicate that upscaling has minimum impact for the sandstones, while for the limestones studied, with significant microporosity that contribute to the flow pathways, the predicted permeability was sensitive to image resolution. The predicted permeabilities—at the highest resolutions—are within a factor of three of the measured values on larger rock samples. This discrepancy is not surprising given the heterogeneous nature of the pore space of these rocks.

6 Conclusions

We have studied the impact of predicted petrophysical properties of using images of different resolution from around 2.7–22 μm . We studied four quarry samples: two sandstones and two limestones.

We showed that network extraction to determine pore and throat size distribution did not produce unique distributions: Increasing the resolution allowed smaller pores and throats to be detected. Furthermore, in the limestones microporosity was not captured at all. There is a poor correspondence between the throat size distributions estimated from a capillary pressure measurement and the extracted throat size distribution.

Despite this, where the image resolution was sufficient to capture most of the pore space, in the sandstones studied, the images gave a good indication of porosity. For limestones with significant microporosity (smaller than the finest resolution), the porosity was significantly underestimated.

We predicted permeability using both direct simulation based on the Navier–Stokes equations on the images and the extracted networks. The methods gave comparable results. This indicates that the network extraction method correctly identified the main flow paths. For the highest resolution images the predictions were comparable to the measurements on larger samples of the same rock. As resolution decreased, the permeability could be substantially under-predicted if connectivity was lost, or over-predicted if the sizes of the main flow pathways were over-estimated.

We recommend that the image resolution used for prediction should be sufficient to resolve most of the pore space: The easiest check is to compare the average throat size of the pore network modeling to the mercury pore size distribution. Another approach would be to compare the measured and imaged porosity and only accept images where the segmented image captures at least 90 % of the porosity. However, these approaches may be complicated by the connectivity of the sample. In some cases, there might be significant fraction of unresolved microporosity which does not contribute to the permeability calculation since the flow is governed by the macro-pores. In other cases, a rock might have small fraction of micropores that do not contribute significantly to the porosity but provide crucial connectivity and hence have a large impact on the permeability.

While the extracted networks could give good predictions of permeability—subject to the constraints above—the extracted pore and throat size distributions are not necessarily in agreement with capillary pressure measurements. This implies that the prediction of multi-phase flow properties, such as capillary pressure and relative permeability may not be reliable. This is a topic of future work.

Acknowledgments We would like to acknowledge funding from the Qatar Carbonates and Carbon Storage Research Centre, QCCSRC, which is supported jointly by Qatar Petroleum, Shell and the Qatar Science and Technology Park.

References

- Al-Kharusi, A.S., Blunt, M.J.: Network extraction from sandstone and carbonate pore space images. *J. Petrol. Sci. Eng.* **56**, 219–231 (2007)
- Alyafei, N., Gharbi, O., Raeini, A.Q., Yang, J., Iglauer, S., Blunt, M.J.: Influence of micro-computed tomography image resolution on the predictions of petrophysical properties. In: *International Petroleum Technology Conference* (2013)
- Arns, C.H., Knackstedt, M.A., Pinczewski, W.V., Garboczi, E.J.: Computation of linear elastic properties from microtomographic images: methodology and agreement between theory and experiment. *Geophysics* **67**(5), 1396–1405 (2002)
- Arns, C.H., Bauget, F., Limaye, A., Sakellariou, A., Senden, T.J., Sheppard, A.P., Sok, R.M., Pinczewski, W.V., Bakke, S., Berge, L.I., Øren, P., Knackstedt, M.A.: Pore scale characterization of carbonates using X-ray microtomography. *SPE J.* **10**(4), 1–10 (2005)
- Ashton, M.: The stratigraphy of the Lincolnshire Limestone Formation (Bajocian) in Lincolnshire and Rutland (Leicestershire). *Proc. Geol. Assoc.* **91**, 203–223 (1980)
- Blunt, M.J., Bijeljic, B., Dong, H., Gharbi, O., Iglauer, S., Mostaghimi, P., Paluszny, A., Pentland, C.: Pore-scale imaging and modelling. *Adv. Water Resour.* **51**, 197–216 (2013)
- Dong, H., Blunt, M.J.: Pore-network extraction from micro-computerized-tomography images. *Phys. Rev. E* **80**(3), 036307 (2009)
- Duchon, C.E.: Lanczos filtering in one and two dimensions. *J. Appl. Meteorol.* **18**(8), 1016–1022 (1979)
- Dunsmuir, J.H., Ferguson, S.R., D’Amico, K.L., Stokes, J.P.: X-ray microtomography: a new tool for the characterization of porous media. In: *SPE Annual Technical Conference and Exhibition* (1991)
- Dullien, F.A.L.: *Porous Media. Fluid Transport and Pore Structure*. Academic, San Diego (1992)
- Gerbaux, O., Buyens, F., Mourzenko, V.V., Momponteil, A., Vabre, A., Thovert, J.-F., Adler, P.M.: Transport properties of real metallic foams. *J. Colloid Interface Sci.* **342**, 155–165 (2010)

- Iglauer, S., Paluszny, A., Pentland, C.H., Blunt, M.J.: Residual CO_2 imaged with X-ray micro-tomography. *Geophys. Res. Lett.* **38**(21), L21403 (2011)
- Iglauer, S., Paluszny, A., Blunt, M.J.: Simultaneous oil recovery and residual gas storage: a pore-level analysis using in situ X-ray micro-tomography. *Fuel* **103**, 905–914 (2013)
- Keemhm, Y., Mukerji, T.: Permeability and relative permeability from digital rocks: Issues on grid resolution and representative elementary volume. In: Society of Exploration Geophysicists (2004)
- Lindquist, W.B., Venkatarangan, A.: Investigating 3D geometry of porous media from high resolution images. *Phys. Chem. Earth Part A* **24**(7), 593–599 (1999)
- Mostaghimi, P., Bijeljic, B., Blunt, M.J.: Simulation of flow and dispersion on pore-space images. *SPE J.* **17**(4), 1131–1141 (2012)
- Münch, B., Trtik, P., Marone, F., Stampanoni, M.: Stripe and ring artefact removal with combined wavelet—Fourier filtering. *Opt. Express* **17**(10), 8567–8591 (2009)
- Øren, P., Bakke, S.: Process based reconstruction of sandstones and prediction of transport properties. *Transp. Porous Media* **46**(2–3), 311–343 (2002)
- Otsu, N.: An automatic threshold selection method based on discriminate and least squares criteria. *Denshi Tsushin Gakkai Ronbunshi* **63**, 349–356 (1979)
- Peng, S., Hu, Q., Dultz, S., Zhang, M.: Using X-ray computed tomography in pore structure characterization for a Berea sandstone: resolution effect. *J. Hydrol.* **472**, 254–261 (2012)
- Pepper, J.F., de Witt, W., Demarest, D.F.: *Geology of the Bedford Shale and Berea Sandstone in the Appalachian basin*. U.S. Geological Survey (1954)
- Raeini, A.Q., Bijeljic, B., Blunt, M.J.: Numerical modelling of sub-pore scale events in two-phase flow through porous media. *Transp. Porous Media* **101**(2), 191–213 (2014)
- Ramstad, T., Idowu, N., Nardi, C., Øren, P.E.: Relative permeability calculations from two-phase flow simulations directly on digital images of porous rocks. *Transp. Porous Media* **94**(2), 487–504 (2012)
- Ryazanov, A.V., van Dijke, M.I.J., Sorbie, K.S.: Two-phase pore-network modelling: existence of oil layers during water invasion. *Transp. Porous Media* **80**(1), 79–99 (2009)
- Santarelli, F.J., Brown, E.T.: Failure of three sedimentary rocks in triaxial and hollow cylinder compression tests. *Int. J. Rock Mech. Min. Sci. Geomech. Abstr.* **26**(5), 401–413 (1989)
- Silin, D.B., Jin, G., Patzek, T.W.: Robust determination of pore space morphology in sedimentary rocks. In: SPE Annual Technical Conference and Exhibition (2003)
- Spanne, P., Thovert, J.F., Jacquin, C.J., Lindquist, W.B., Jones, K.W., Adler, P.M.: Synchrotron computed microtomography of porous media: topology and transports. *Phys. Rev. Lett.* **73**(14), 2001–2004 (1994)
- Tanino, Y., Blunt, M.J.: Capillary trapping in sandstones and carbonates: dependence on pore structure. *Water Resour. Res.* **48**(8), W08525 (2012)
- Thovert, J.-F., Yousefian, F., Spanne, P., Jacquin, G.G., Adler, P.M.: Grain reconstruction of porous media: application to a low-porosity Fontainebleau sandstone. *Phys. Rev. E* **63**, 061307 (2001)
- Tschumperlé, D., Deriche, R.: Vector-valued image regularization with PDE's: a common framework for different applications. *IEEE Trans. Pattern Anal. Mach. Intell.* **27**(4), 506–517 (2005)
- Valvatne, P.H., Blunt, M.J.: Predictive pore-scale modeling of two-phase flow in mixed wet media. *Water Resour. Res.* **40**(7), W07406 (2004)
- Wildenschild, D., Sheppard, A.P.: X-ray imaging and analysis techniques for quantifying pore-scale structure and processes in subsurface porous medium systems. *Adv. Water Resour.* **51**, 217–246 (2013)
- Wildenschild, D., Vaz, C.M.P., Rivers, M.L., Rikard, D., Christensen, B.S.B.: Using X-ray computed tomography in hydrology: systems, resolutions, and limitations. *J. Hydrol.* **267**(3), 285–297 (2002)
- Wildenschild, D., Hopmans, J.W., Rivers, M.L., Kent, A.J.R.: Quantitative analysis of flow processes in a sand using synchrotron-based X-ray microtomography. *Vadose Zone J.* **4**(1), 112–126 (2005)
- Wright, V.P., Platt, N.H., Marriott, S.B., Beck, V.H.: A classification of rhizogenic (root-formed) calcretes, with examples from the Upper Jurassic-Lower Cretaceous of Spain and Upper Cretaceous of southern France. *Sed. Geol.* **100**, 143–158 (1995)